Title

Radiofrequency transmit calibration: A multi-center evaluation of vendor-provided radiofrequency transmit mapping methods

Journal

Medical Physics, 46(6)

ISSN

0094-2405

Authors

Bliesener, Yannick
Zhong, Xinran
Guo, Yi
et al.

Publication Date

2019-06-01

DOI

10.1002/mp.13518

Peer reviewed

Radiofrequency transmit calibration: A multi-center evaluation of vendor-provided radiofrequency transmit mapping methods

Yannick Bliesener
Ming Hsieh Department of Electrical Engineering, Viterbi School of Engineering, University of Southern California, Los Angeles, CA, USA

Xinran Zhong
Department of Radiological Sciences & Physics and Biology in Medicine IDP, University of California Los Angeles, Los Angeles, CA, USA

Yi Guo
Ming Hsieh Department of Electrical Engineering, Viterbi School of Engineering, University of Southern California, Los Angeles, CA, USA

Michael Boss
Applied Physics Division, National Institute of Standards and Technology, Boulder, CO, USA

Ryan Bosca
Imaging Physics, Sanford Health, Fargo, ND, USA

Hendrik Laue
Institute for Medical Image Computing, Fraunhofer MEVIS, Bremen, Germany

Caroline Chung
Radiation Oncology and Radiology, The University of Texas MD Anderson Cancer Center, Houston, TX, USA

Kyunghyun Sung
Department of Radiological Sciences & Physics and Biology in Medicine IDP, University of California Los Angeles, Los Angeles, CA, USA

Krishna S. Nayak[a)]
Ming Hsieh Department of Electrical Engineering, Viterbi School of Engineering, University of Southern California, Los Angeles, CA, USA

(Received 25 October 2018; revised 21 February 2019; accepted for publication 18 March 2019; published 15 April 2019)

Purpose: To determine the accuracy and test-retest repeatability of fast radiofrequency (RF) transmit measurement approaches used in Dynamic Contrast Enhanced Magnetic Resonance Imaging (DCE-MRI). Spatial variation in the transmitted RF field introduces bias and increased variance in quantitative DCE-MRI metrics including tracer kinetic parameter maps. If unaccounted for, these errors can dominate all other sources of bias and variance. The amount and pattern of variation depend on scanner-specific hardware and software.
Methods: Human tissue mimicking torso and brain phantoms were constructed. RF transmit maps were measured and compared across eight different commercial scanners, from three major vendors, and three clinical sites. Vendor-recommended rapid methods for RF mapping were compared to a slower reference method. Imaging was repeated at all sites after 2 months. Ranges and magnitude of RF inhomogeneity were compared scanner-wise at two time points. Limits of Agreement of vendor-recommended methods and double-angle reference method were assessed.
Results: At 3 T, B_1^+ inhomogeneity spans across 35% in the head and 120% in the torso. Fast vendor provided methods are within 30% agreement with the reference double angle method for both the head and the torso phantom.
Conclusions: If unaccounted for, B_1^+ inhomogeneity can severely impact tracer-kinetic parameter estimation. Depending on the scanner, fast vendor provided B_1^+ mapping sequences allow unbiased and reproducible measurements of B_1^+ inhomogeneity to correct for this source of bias. © *2019 American Association of Physicists in Medicine* [https://doi.org/10.1002/mp.13518]

Key words: DCE-MRI, RF transmit, RF inhomogeneity, high field, quantitative MRI

1. INTRODUCTION

Magnetic resonance imaging (MRI) utilizes radiofrequency (RF) fields for both excitation and reception of signal from tissue. The RF transmit (also called B_1^+) field used for excitation is generated typically by a body coil or, in special circumstances, by local transmit/receive coils. Spatial variation in the magnitude of the B_1^+ field causes spatial variation in the imaging flip angle,[1,2] which can be particularly problematic for quantitative MRI, including dynamic contrast enhanced (DCE) imaging.[3,4]

The spatial variation in the B_1^+ field has been well-studied at 1.5, 3, and 7 T. The amount of variation is greater at higher field strengths and for objects with larger physical dimensions (e.g., abdomen vs head). This is largely attributed to dielectric effects and wavelength effects. Note that the ^{1}H RF wavelength in human tissue is approximately 26 cm at 3 T and 11 cm at 7 T.[2,5,6] B_1^+ spatial variation at 1.5 T is negligible in human head and musculoskeletal imaging, but can be substantial in the torso.[7,8] At 3 T and above, the effects of B_1^+ variation have been observed in all body regions and is significant.[3,4,9–11] The interest in measuring and characterizing B_1^+ variation significantly increased around 2003, when 3 T MRI first received FDA clearance.

Spatial B_1^+ variation is impacted by the geometry and algorithms for driving the body RF coil, and therefore expected to be platform dependent. Early 3 T scanners used circularly polarized body coils. The next generation used elliptical polarization with a fixed phase. Recent scanners include elliptical polarization with subject-dependent phase that is determined through a calibration scan. Each of these developments has improved the uniformity of the RF transmit field in vivo.[7]

Quantitative DCE-MRI is the main motivating application of this work and involves two steps that are sensitive to flip angle errors: (a) pre-contrast T_1 mapping and (b) conversion of DCE-MRI *signal intensity* to *contrast agent concentration*. If unaccounted for, the flip angle errors caused by B_1^+ spatial variation propagates to DCE-MRI tracer kinetic maps and produces substantial errors. These errors hamper the reproducibility and utility of quantitative DCE-MRI in clinical trials.

The impact of B_1^+ inhomogeneity on DCE-MRI has been studied in head, breast, prostate, heart, and abdomen. In the head, Sengupta et al.[4] showed that lack of B_1^+ correction at 3 T can lead to over- and under-estimation of concentration time curves and K^{trans} parameters depending on the location of the tumor region of interest (ROI) relative to the B_1^+ profile. They further demonstrated through simulation how these variations can have the potential to alter tumor classification.

For breast DCE-MRI, one team[12–14] documented up to 50% lower than expected flip angle at 3 T. This alone resulted in up to 66% and 74% underestimation of K^{trans} and v_e. Semi-quantitative indices such as enhancement ratio and relative enhancement ratio were designed to be less sensitive to RF transmit variation. Another team[3] documented 33% variation in flip angle in bilateral breast imaging, and demonstrated that its measurement could be used to improve pre-contrast T_1 maps. Gruber et al.[15] documented 50% and 19% flip angle variation in bilateral breast MRI, at 7 and 3 T, respectively. The most significant deviations at 7 T were in the prepectoral and lateral regions of the breast.

In prostate, Fennessy et al.[9] demonstrated through simulations and experiments that flip angle variation resulted in significant errors in pre-contrast T_1 mapping. 40% variations would result in inability to differentiate tumor and normal tissue. Rangwala et al.[16] has documented around 10—15% intra-subject variation across the prostate, up to 30% inter-subject variation in flip angle, and up to 15% inter-scanner variation across three Siemens MRI scanners. In the heart, Greenman et al.[10] observed B_1^+ variation in nearly 100% in the anterior/posterior direction at 3 T, Sung et al.[11] measured B_1^+ variation in up to 63% over the entire left ventricle volume, and Ruan et al.[17] list RF transmit inhomogeneity as one of the major confounding factors for cardiac perfusion MRI. Finally, in the abdomen Treier et al.[18] demonstrated improvements in variable-flip angle T_1 mapping by using a B_1^+ map to correct spatial variations in nominal flip angle.

With knowledge of B_1^+, the effect of spatial variation can be compensated. The typical approach is to perform a separate scan to measure the spatial variation in the amplitude of the RF transmit field, and then incorporate the spatially varying flip angle during conversion of DCE-MRI image series into contrast agent concentration image series, prior to kinetic modeling. Some kinetic modeling software performs the signal-intensity to concentration conversion, so this would need to be integrated. There are several MRI pulse sequences for measuring the RF transmit field, most notably the Double Angle Method (DAM),[19,20] Actual Flip Angle Imaging (AFI),[21] Bloch-Siegert Method,[22] preconditioned RF,[23] and Dual Refocusing Echo Acquisition Mode (DREAM).[24] Each of these methods has variants that are not practical to cite individually, and many can be performed in under 2 min. The optimal method is expected to depend on the body part, the expected amount of variation over the imaging volume, and physiological factors such as motion and flow.

This study designed two head and two torso phantoms that matched conductivities in human tissue with short and long longitudinal relaxivities. We then performed a multi-center and multi-vendor assessment of B_1^+ inhomogeneity (eight MRI scanners with three vendors) at two time points to compare agreement of fast vendor B_1^+ measurement methods and the impractically slow double angle reference method.

2. MATERIALS AND METHODS

2.A. Phantom construction

A spherical head phantom (Diffusion Phantom Shell, High Precision Devices, Boulder, CO, USA) and a custom torso phantom (Shelley Medical Imaging Technologies, North York, Ontario, Canada) were used in this study. The torso shaped phantom was approximately the size of a human adult

torso with a concentric outer shell, creating one large fillable interior volume and one smaller fillable outer volume to mimic subcutaneous adipose tissue. The outer volume of the torso phantoms was filled with a commercial fat-mimicking solution with T_1 of approximately 350 ms (Fat Mimic L9010, High Precision Devices, Boulder, CO, USA). The human adult head-sized phantom had a single interior fillable volume. Two versions of each phantom were created and the interior volumes were filled with two different solutions, resulting in a total of four phantoms.

B_1^+ inhomogeneity was not expected to be a function of T_1, however, the performance of B_1^+ mapping techniques could be influenced by T_1. These two interior solutions cover the range of short and long T_1s expected in organ tissue during a DCE-MRI acquisition with current recommended contrast agent dosage. We designed the first to achieve a uniform T_1 of approximately 1.5 s at 3 T (0.543 mM $NiCl_2$), and the second to achieve a uniform T_1 of approximately 300 ms at 3 T (4.844 mM $NiCl_2$). The conductivity of both solutions was matched to that of human tissue (40 mM NaCl).[6] Concentrations are listed in Table S1 in the supplementary material.

2.B. Verification of the T_1 values

Aliquots of each fill solution were reserved and sent to NIST for independent analysis. At NIST, samples were sealed in 1.9 mm borosilicate capillaries, and placed in a standard 5 mm NMR tube next to a fiber optic thermometer probe to allow *in situ* thermometry and temperature control. T_1 values were evaluated on a 3 T NMR spectrometer using inversion recovery with TR $>5T_1$ for all samples over all experiments. Data were collected at 15°C, 20°C, and 25°C in triplicate and fitted; results from the curve fits were averaged to determine mean values and standard deviations of the relaxation times.

2.C. Data collection

The four phantoms were scanned on eight MRI scanners, listed in Table I. For each scanner, MRI scans were performed on two separate occasions, ranged from 2 to 7 months. There have been no software or hardware alterations during the time of the data acquisition for this study.

The B_1^+ mapping methods, listed in Table I, included vendor-recommended methods that were provided in response to a survey given to the vendor subcommittee of the Radiological Society of North America (RSNA) Quantitative Imaging Biomarkers Alliance (QIBA) between March and June 2016 or have been chosen in consultation with vendor engineers. The clinically available 2D DAM was used as the reference standard. Parameters and approximate scan times for all B_1^+ mapping methods that are used throughout this study are summarized in Table II.

Upon arrival at the scan site, all phantoms were unpacked to adapt to room temperature. Before the scan session the temperature of the phantoms was measured to be about 20°C using an infrared thermometer (FLIR ONE Gen 1, FLIR Systems Inc., Wilsonville, OR, USA). After positioning each fluid-filled phantom, we waited ~5 min for internal flows to stabilize. T_1 mapping was performed at the end of each scan session. Scan time was roughly 12–30 min for the DAM scans, and roughly 2 min for the vendor-recommended method, on each MRI platform.

TABLE I. Summary of scanners and sites participating in this study. Sites were chosen based on research access and proximity (all in the Los Angeles metro area).

ID	Vendor	B0	Model	Software	Location	Method
S1	Siemens	1.5 T	Avanto	VE11	UCLA	Saturated FLASH[23]
S2	Siemens	3 T	Skyra	VE11	UCLA	Saturated FLASH[23]
S3	Siemens	3 T	Prisma	VE11	UCLA	Saturated FLASH[23]
S4	Siemens	3 T	Prisma	VE11	UCLA	Saturated FLASH[23]
G1	GE	3 T	HD23	24.0	USC/Keck	Bloch-Siegert[22]
G2	GE	3 T	HD23	24.0	USC/Keck	Bloch-Siegert[22]
G3	GE	3 T	HD23	24.0	USC/Keck	Bloch-Siegert[22]
P1	Philips	3 T	Achieva	5.3.0	CHLA	DREAM[24]

UCLA, University of California at Los Angeles David Geffen School of Medicine; USC/Keck, University of Southern California Keck School of Medicine; CHLA, Children's Hospital Los Angeles; DREAM, dual refocusing echo acquisition mode.

TABLE II. Imaging Parameters for each B_1^+ mapping method. Double Angle Method (DAM) parameters were chosen to keep them consistent across scanners while maximizing SNR and avoiding parameter conflicts. Parameters for vendor methods follow recommended settings of the respective vendor.

Method/Parameter	Torso	Head
FOV	400 × 400 mm^2	240 × 240 mm^2
Slice thickness	8 mm	8 mm
Slice gap	2 mm	2 mm
Matrix	64 × 64	64 × 64
Double angle (Reference)		
FA	45°/90°	45°/90°
TR	6000 ms	6000 ms
Scan time	12–27 min	12–18 min
satTFL (Siemens)		
FA	80°	80°
Scan time	20 s	20 s
Bloch-Siegert (GE)		
FA	15°	15°
TE/TR	12.1/41 ms	12.1/41 ms
Scan time	<2 min	<1 min
DREAM (Philips)		
FA	20°	5°
STEAM	55°	45°
Scan time	<2 min	<2 min

DREAM, dual refocusing echo acquisition mode.

2.D. Data analysis

Data analysis was performed based on regions of interest (ROIs). To this end, ROIs were determined based on 45° scans for the DAM B_1 mapping. For the head phantoms two axial slices to either end of the central grid were selected as close as possible to the center of the phantom such that no residual of the central grid was visible in the slices. The convex hull of the edges detected by Matlab®'s Sobel method were eroded with disk sizes of 4, 7, and 5 pixels for GE, Siemens, and Philips to exclude voxels affected by partial volume averaging and to generate the ROIs for further analysis. For the torso phantom, three axial slices were chosen: one central slice and two slices to either end of the phantom. Positions for the distal slices were chosen to avoid apparent T_1 roll-off as detected by the inspection of coronal B_1-corrected T_1 maps. ROIs were automatically generated using the Matlab®'s Fast-Marching-Method operated on the second derivative of the image. As for the head phantom, the ROIs were subsequently eroded by two pixels for GE and Philips and three pixels for Siemens. As some slices did not fully resolve the fat-water boundary in the torso phantom, the ROIs were manually adjusted as a last step.

Individual B_1^+ maps were analyzed to determine ranges and magnitude of B_1^+ inhomogeneity. B_1^+ inhomogeneity was defined as percentage of measured flip angle relative to prescribed flip angle. Ranges of deviation are based on 5% and 95% percentiles in the ROI. Magnitude of inhomogeneity was assessed based on standard deviation within the ROI. Due to symmetry both slices were combined for the head phantom, while for the torso phantom analysis was done separately for the central and the distal slices.

Agreement of vendor specific methods with DAM measurements is assessed based on Limits of Agreement (LOA) which incorporate information about bias and variance.[25] The LOA are computed as the interval of range equal to twice the coefficient of reproducibility (RDC) and centered about the mean difference between the two methods. We further used concordance correlation coefficients to determine reproducibility of the B_1^+ maps by the vendor specific methods.

Analyzing repeatability on a pixelwise basis requires exact positioning of the phantom relative to the excitation coils. Due to the symmetry of the phantoms and fixed mounting of the head coil, this is achieved more easily for the head phantom. We therefore compare repeatability of DAM and vendor methods pixelwise for the head phantom. To further determine repeatability of agreement between DAM and vendor methods, the data analysis with LOA was repeated identically for the second round of measurements, and results were compared between the two time points.

3. RESULTS

3.A. Phantom properties

Figure 1 shows two fabricated phantom geometries: the head phantom for the long T_1 and the torso phantom for the short T_1. Table S2 in the supplementary material summarizes results of T_1 value verification for short and long T_1 phantoms. The measured T_1 values were all within 15% of theoretical values at 20°C. The apparent lack of temperature dependence for the short T_1 measurements is due to the relatively weak influence of temperature on the relaxivity of Ni^{2+}. The stronger relaxation at a higher concentration of nickel dominates the intrinsic relaxation contribution from the water molecules. At low nickel (long T_1), the temperature-dependence of water's relaxation rate is more readily apparent, and more strongly influences the aggregate T_1 as a function of temperature.

3.B. B_1^+ spatial variation

Figure 2 shows representative spatial maps of B_1^+ inhomogeneity measured by DAM for the head phantom. Table S3 in the supplementary material summarizes ranges and magnitude of inhomogeneity. Due to its lower field strength, scanner S1 has an overall flatter B_1^+ profile compared to the 3 T scanners with a maximum range of deviation of 8.2%. While the T_1 value of the head phantom had little impact on the measured B_1^+ inhomogeneity, magnitude of inhomogeneity was vendor dependent. Among the 3 T scanners, Siemens scanners exhibit the overall lowest B_1^+

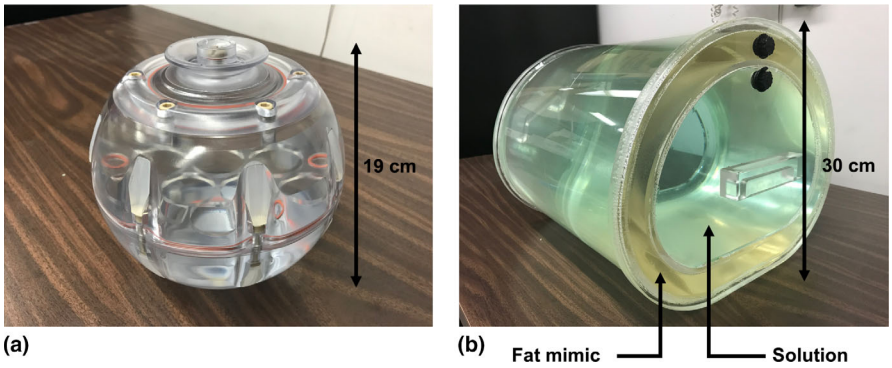

FIG. 1. Spherical head phantoms (a) and custom torso phantoms (b) were used in this study. The human adult head-sized phantom had a single interior fillable volume. The torso shaped phantom was approximately the size of a human adult torso with a concentric outer shell, creating one large fillable interior volume and one smaller fillable outer volume to mimic subcutaneous adipose tissue. The outer volume of the torso phantoms was filled with a commercial fat-mimicking solution. [Color figure can be viewed at wileyonlinelibrary.com]

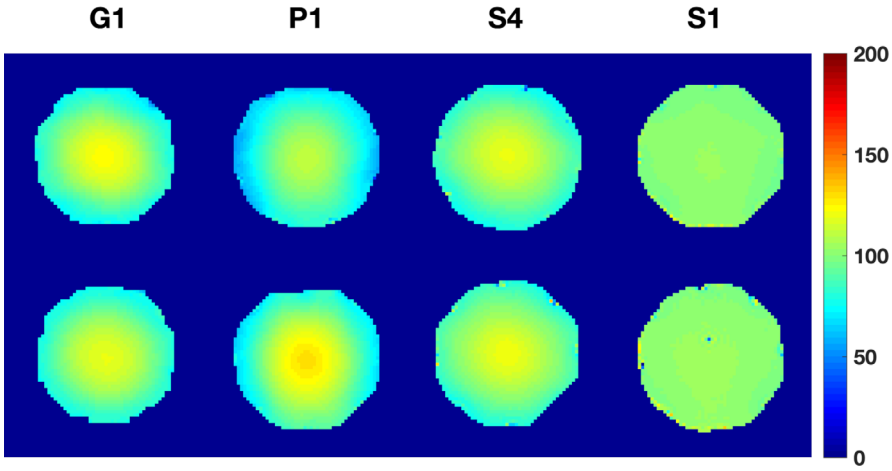

FIG. 2. Selected (typical) spatial B_1^+ maps acquired with Double Angle Method (DAM) for the short (top row) and long T_1 head phantoms (bottom row). While Siemens and GE show small dependence of the B_1^+ mapping method on the T_1 value, Philips DAM shows a slightly stronger dependence. As expected, S1 with its lower field strength (B_0 = 1.5 T) has a flatter B_1^+ profile. [Color figure can be viewed at wileyonlinelibrary.com]

inhomogeneity with a maximum range of 30.5%, followed by GE with 31.2%, and Philips with 41.8%.

Figure 3 shows selected B_1^+ inhomogeneity maps for torso phantoms measured by the DAM, while Table S4 in the supplementary material summarizes ranges and magnitudes of deviation for the short and long T_1 phantoms for a central and the two distal slices. The overall B_1^+ inhomogeneity is more severe in the bigger torso phantom compared to the smaller head phantom. As for the head phantom, the Siemens scanner S1 operating at 1.5 T exhibits the flattest B_1^+ profile with a maximum range of 26.2%. In contrast to the head phantom, B_1^+ maps acquired with the DAM show a much stronger dependence on the phantom T_1 value. With the exception of GE scanner G3, all scanners measure stronger B_1^+ inhomogeneity at the longer T_1 value. Maximum range of inhomogeneity at 3 T was 111.3% for Siemens scanners, 124.3% for GE, and 115.8% for the Philips scanner. There seems to be no substantial difference in terms of B_1^+ inhomogeneity between the central slice and the two distal slices.

3.C. Agreement of vendor-provided fast B_1^+ mapping with DAM

Figure 4 illustrates scatter plots for agreement of DAM B_1^+ measurements with vendor specific methods for a representative selection of scanners. Metrics of reproducibility in round 1 data are summarized in Table S5 in the supplementary material for the head phantom studies and in Table S6 in the supplementary material for the torso phantom studies.

With the exception of Siemens scanner S2, Siemens scanners show overall best agreement of reference DAM with vendors methods both in terms of LOA and CCC. Among the 3 T scanners, the LOA indicate overall very low bias between DAM and satTFL on Siemens scanners. Siemens' satTFL measures higher B_1^+ inhomogeneity at higher T_1 values in the head phantom as can be observed by larger RDC values and lower CCC, while good agreement between both methods is achieved irrespective of the T_1 value and slice location for the torso phantom. For GE scanners, largely varying LOA

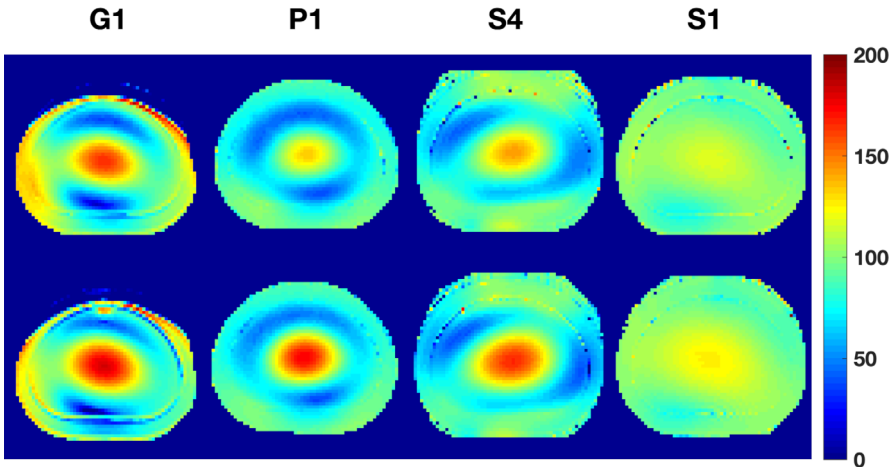

FIG. 3. Selected (typical) spatial B_1^+ maps acquired with the double angle method for the short (top row) and long T_1 torso phantoms (bottom row). Most scanners measured higher B_1^+ heterogeneity at the longer T_1. As expected, S1 with its lower field strength (B_0 = 1.5 T) has a flatter B_1^+ profile, yet there is a higher T_1 dependence than for the head phantom. [Color figure can be viewed at wileyonlinelibrary.com]

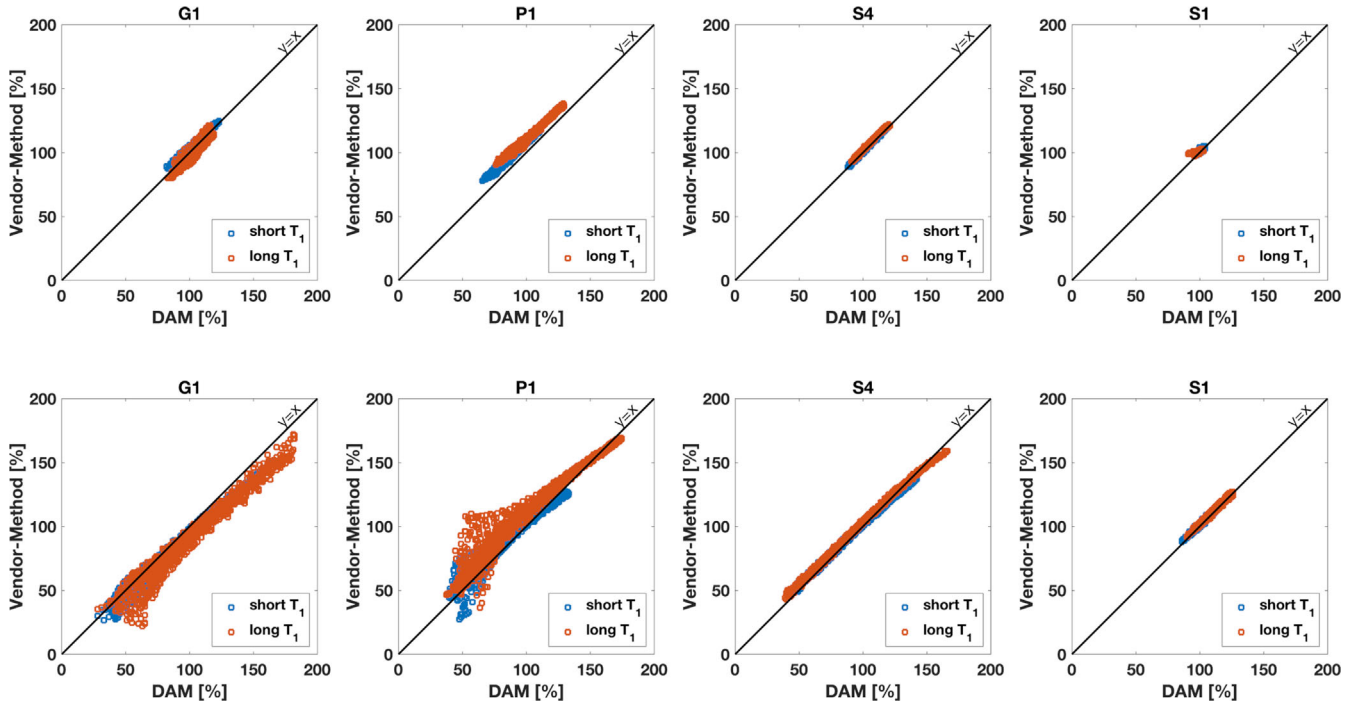

FIG. 4. Selected correlation plots for head phantoms (top row) and torso phantoms (bottom row). Correlation is shown between Double Angle Method (DAM) reference method and the respective vendor-specific fast B_1^+ mapping method. For the head phantoms, all vendor methods show excellent agreement with DAM. For the torso phantoms, Siemens' satTFL shows good agreement with DAM, while Philips' and GE's method exhibit deviations from DAM in presence of large B_1^+ heterogeneity. [Color figure can be viewed at wileyonlinelibrary.com]

and CCC show that agreement of Bloch-Siegert method and DAM are very device specific for both the smaller head phantom and the larger torso phantom. The one Philips scanner used in this study exhibited LOA and CCC for agreement of DAM with DREAM comparable to results found on GE systems, while bias and variance of DREAM were consistently higher at long T_1 phantoms.

3.D. Two-month repeatability

Figure 5 shows voxel-wise test-retest repeatability of measured B_1^+ using the head phantom for a selection of scanners. Despite potential inaccuracies due to irreproducibility of the exact relative positioning of phantom and excitation coils, both DAM and vendor methods exhibit good agreement across repeated scans.

Tables S7 and S8 in the supplementary material list results of the repeated measurements during round 2 for the head phantoms and for the torso phantoms, respectively. Comparing head phantom measurements during round 1 (Table S5 of supplementary material) and round 2 (Table S7) reveals very similar performance for Siemens and Philips scanners at both time points. As for the first time point, Siemens scanners show the overall smallest bias between DAM and vendor specific method. Siemens scanner S2 has a largely increased RDC for both the short and long T_1 head phantom which results from deviation of the DAM and satTFL at the boundary of the ROI (see head/summaryHead.html in supplementary material). The comparison of round 2 data for the torso phantoms (Table S6 of supplementary material) to round 1 data (Table S8) shows the same stability of measurements for repeated measurements for Siemens and Philips scanners as it did for the head phantoms. For GE scanners, round 2 confirms the large variation in LOA and CCC across devices.

3.E. Archived data

The supplementary material to this manuscript contains Tables S2–S8, spatial maps, histograms of differences, agreement plots, and Bland-Altman plots to the data listed in Tables S3–S8. The supplementary material consists of two html-files, *head/summaryHead.html* and *torso/summaryTorso.html*, that display all figures.

The data acquired in this study is available in the Quantitative Imaging Data Warehouse (QIDW) hosted by RSNA (https://qidw.rsna.org/) in following folder: Collections/MR Modality Datasets/Dynamic Contrast Enhanced (DCE) MRE/DCE Profile Supporting Data/ Nayak DCE Phantom Data.

4. DISCUSSION

This study aimed at comparing double-angle reference B_1^+ mapping with various faster vendor provided methods on different scanners and at different time points. We therefore constructed four phantoms to cover two important body parts, and to cover end points of the spectrum of T_1 values that are typical in the human body. As the actual B_1^+ map does not depend on the specific T_1 value, the latter was done to assess if the B_1^+ mapping methods are insensitive to T_1.

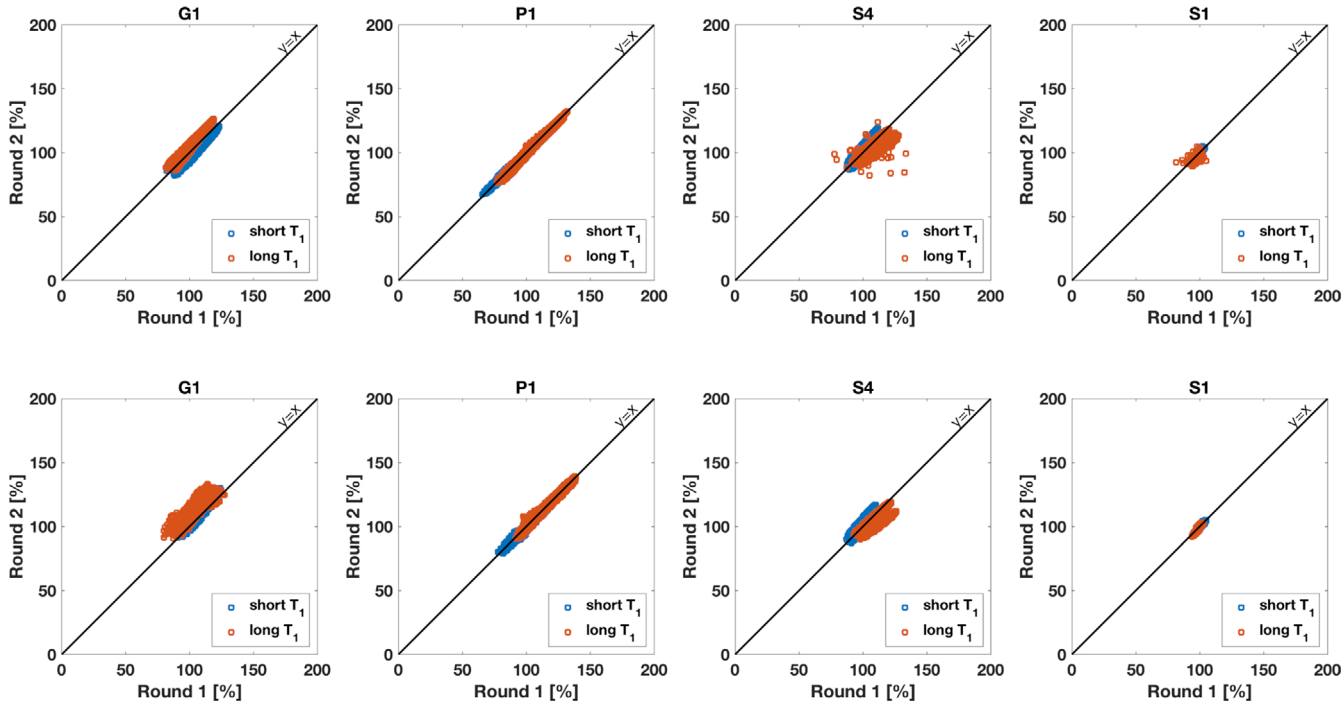

FIG. 5. Selected correlation plots showing repeatability of voxel-wise B_1^+ in head phantoms: Double Angle Method (top row) and vendor methods (bottom row). Correlation is shown between first scan and the second scan, which had a time gap of at least 2 months. Scanner hardware, software, and imaging protocol were identical at both time points. [Color figure can be viewed at wileyonlinelibrary.com]

At 3 T, Siemens scanners showed the overall flattest B_1^+ profiles with a maximum range of 30.5% for the head phantom and 111.3% for the torso. GE scanners had a maximum range of 31.2% for the head and 124.3% for the torso, while for the Philips scanner these ranges amount to 41.8% and 115.8%, respectively. For the head phantom the DAM measurements exhibited mildly higher variation in the B_1^+ profile at the higher T_1 value on all but one scanner, while for the torso phantom this trend was stronger pronounced on all but one scanner. Siemens scanners have the lowest mean difference between DAM and vendor specified method, which could be achieved irrespective of the T_1 value for the torso phantom, but with increased variance for the long T_1 head phantom. For GE scanners, agreement was highly variable across scanners. Philips' DREAM method showed higher mean and variance of differences to DAM at longer T_1 irrespective of the phantom size. Repeated measurements revealed performance of Siemens and Philips scanners to be consistent across repeated exams. While there are mild differences in the speed of the vendor-specific B_1^+ mapping method with Siemens' being the fastest, followed by GE's and Philips', no vendor method was found to be prohibitively slow to not be included in a clinical protocol.

Through simulation and verification experiments, Tropp[26] predicted B_1^+ inhomogeneity of spherical phantoms with comparable size at 3 T with aqueous NaCl solution of similar conductivity (radius 9.25 cm, conductivity 0.5 S/m) to our study, and found pattern of central enhancement in good qualitative agreement with our results. Sengupta et al.[4] performed a similar study to assess the effect of B_1^+ inhomogeneity on perfusion and permeability parameters in head DCE-MRI. This study examined B_1^+ inhomogeneity on a 3 T Ingenia Philips scanner and reported B_1^+ inhomogeneity in the range of 85%–125% across multiple patients. This is in good agreement with our results for the Philips scanner P1 for the long T_1 head phantom which is close to the typical T_1 values for white and gray matter found in the brain. Jiru et al.[27] used a modified AFI method to obtain spatial B_1^+ inhomogeneity maps on a 3 T Trio Tim Siemens scanner which are qualitative similar to head phantom maps in this study, yet show a slightly lower range of approximately 80% to 110%.

In prostate DCE-MRI, Fennessy et al.[9] found a dynamic range of 60–140% inhomogeneity of B_1^+ in a small ROI of the pelvic muscle on a GE scanner across different patients with assumed knowledge of muscle T_1 = 1420 ms by fitting VFA data. This, again, is in good agreement with our results found in the long T_1 torso phantom despite the much larger ROI in our study. Considering that the pelvic muscle ROI was typically chosen to the left or right of the field of view (FOV) center it is easy to see in the spatial B_1^+ maps how such an ROI might fall onto a falling edge of the central B_1^+ inhomogeneity enhancement, which could explain the dynamic range even in a much smaller ROI.

Rangwala et al.[16] optimized reference region VFA (RR-VFA) to measure T_1 maps alongside B_1^+ inhomogeneity in prostate on three Siemens scanners (3 T). The illustrated B_1^+ inhomogeneity maps exhibit qualitatively different behavior from the ones obtained on the phantoms in this study, yet the overall dynamic range of inhomogeneity is similar. The lack of the characteristic B_1^+ inhomogeneity enhancement at the object center may be attributed to heterogeneity in the electro-

magnetic properties of the various tissue specimen in the pelvis which give rise to more complicated resonant mode formations.

This study used unusually large ROIs for the analysis of B_1^+ inhomogeneity both in case of the head phantoms and the torso phantoms. In clinical applications ROIs more typically span smaller areas of the FOV that cover organs such as prostate, liver, or kidney. While B_1^+ inhomogeneity across these smaller regions is of great interest it would have been impractical for this comprehensive study to do separate analysis for each of these cases. The interested reader can access the measured data from the QIBW database to perform such analysis for their specific ROI.

Commercial MRI technology is constantly evolving. It was not practical for this study to include all available MRI scanners. Scanners as well as vendor recommended B_1^+ mapping tools need to be available and accessible for this kind of study which can pose significant obstacles. In the vein of reproducible research and to potentially expand the pool of scanners that are investigated, the phantoms will be maintained by our laboratory for 2 yrs and can be loaned upon request.

Another limitation of this study is the lack of direct, pixelwise comparison of repeated measurements for DAM and the vendor specific methods. Since B_1^+ inhomogeneity on the voxel level depends highly on the position of the object under investigation relative to the transmit coil position, positioning phantoms and ROIs to measure the exact position twice is very challenging. Misplacement introduces variation in the measurement that is unrelated to the performance of the respective method. To get around this potential source of error while still assessing robustness of measurements across repetitions we chose to compare aggregated statistics at two time points. We do not believe that this poses a major limitation to the interpretation of the results as due to said issues during positioning B_1^+ maps are typically measured for each patient prior to each DCE-MRI exam regardless.

Datasets like the present can be used for error propagation analysis to determine the effect of B_1^+ heterogeneity on the estimates of interest such as tracer-kinetic parameters in DCE-MRI exams. We plan to perform such analysis and present results in a follow-up paper.

5. CONCLUSION

We designed and constructed head and torso phantoms for verification of B_1^+ inhomogeneity measurement methods in a multi-center, multi-vendor study. Vendor-provided fast methods perform within 26% agreement of the slow double angle reference method for head and within 30% for torso phantoms. Mean range of B_1^+ inhomogeneity is 103% and 25% for the torso at 3 and 1.5 T, respectively, and 30% and 7% for brain at 3 and 1.5 T, respectively. This results in a proportional variation in DCE-MRI derived tracer-kinetic parameters if B_1^+ variation is not accounted for, and if protocols are designed to stay in the linear contrast agent vs signal intensity regime (more nuanced error propagation analysis is forthcoming). B_1^+ mapping is expected to be an important part of pre-scan calibration for DCE-MRI.

ACKNOWLEDGMENTS

This study was supported as a RSNA-QIBA Round 6 Groundwork Project funded in part by the NIH/NIBIB under contract no. HHS-N268201500021C. We thank John Kirsch, R. Marc Lebel, Hans Peeters, Kay Nehrke, Peter Börnert, Samir Sharma, Nancy Obuchowski, and all members of the QIBA DCE-MRI Task Force that provided guidance and/or helpful discussions.

CONFLICT OF INTEREST

The authors have no relevant conflict of interest to disclose.

[a)]Author to whom correpsondence should be addressed. Electronic mail: knayak@usc.edu; Telephone: 213-740-3494; Fax: 213-740-4651.

REFERENCES

1. Vaughan JT, Garwood M, Collins CM, et al. 7T vs 4T: RF power, homogeneity, and signal-to-noise comparison in head images. *Magn Reson Med*. 2001;46:24–30.
2. Webb AG, Collins CM. Parallel transmit and receive technology in high-field magnetic resonance neuroimaging. *Int J Imaging Syst Technol*. 2010;20:2–13.
3. Sung K, Daniel BL, Hargreaves BA. Transmit B_1^+ field inhomogeneity and T1 estimation errors in breast DCE-MRI at 3 tesla. *J Magn Reson Imaging*. 2013;38:454–459.
4. Sengupta A, Gupta RK, Singh A. Evaluation of B1 inhomogeneity effect on DCE-MRI data analysis of brain tumor patients at 3T. *J Transl Med*. 2017;15:1–13.
5. Noeske R, Seifert F, Rhein KH, Rinneberg H. Human cardiac imaging at 3 T using phased array coils. *Magn Reson Med*. 2000;44:978–982.
6. Gabriel S, Lau RW, Gabriel C. The dielectric properties of biological tissues : II. Measurements in the frequency range 10 Hz to 20 GHz. *Phys Med Biol*. 1996;41:2251–2269.
7. Soher BJ, Dale BM, Merkle EM. A review of MR physics: 3T versus 1.5T. *Magn Reson Imaging Clin N Am*. 2007;15:277–290.
8. Sled JG, Pike GB. Correction for B1 and B0 variations in quantitative T2 measurements using MRI. *Magn Reson Med*. 2000;43:589–593.
9. Fennessy FM, Fedorov A, Gupta SN, Schmidt EJ, Tempany CM, Mulkern RV. Practical considerations in T1 mapping of prostate for dynamic contrast enhancement pharmacokinetic analyses. *Magn Reson Imaging*. 2012;30:1224–1233.
10. Greenman RL, Shirosky JE, Mulkern R V, Rofsky NM. Double inversion black-blood fast spin-echo imaging of the human heart: a comparison between 1.5T and 3.0T. *J Magn Reson Imaging*. 2003;17:648–655.
11. Sung K, Nayak KS. Measurement and characterization of RF nonuniformity over the heart at 3T using body coil transmission. *J Magn Reson Imaging*. 2008;27:643–648.
12. Di Giovanni P, Azlan CA, Ahearn TS, Semple SI, Gilbert FJ, Redpath TW. The accuracy of pharmacokinetic parameter measurement in DCE-MRI of the breast at 3 T. *Phys Med Biol*. 2010;55:121–132.
13. Azlan CA, Di Giovanni P, Ahearn TS, Semple SIK, Gilbert FJ, Redpath TW. B1 transmission-field inhomogeneity and enhancement ratio errors in dynamic contrast-enhanced MRI (DCE-MRI) of the breast at 3T. *J Magn Reson Imaging*. 2010;31:234–239.

14. Azlan CA, Ahearn TS, Di Giovanni P, Semple SIK, Gilbert FJ, Redpath TW. Quantification techniques to minimize the effects of native T1 variation and B1 inhomogeneity in dynamic contrast-enhanced MRI of the breast at 3 T. *Magn Reson Med*. 2012;67:531–540.
15. Gruber S, Pinker K, Zaric O, et al. Dynamic contrast-enhanced magnetic resonance imaging of breast tumors at 3 and 7 T. *Invest Radiol*. 2014;49:354–362.
16. Rangwala NA, Dregely I, Wu HH, Sung K. Optimization and evaluation of reference region variable flip angle (RR-VFA) B1 + and T1Mapping in the Prostate at 3T. *J Magn Reson Imaging*. 2017;45:751–760.
17. Ruan C, Yang SH, Cusi K, Gao F, Clarke GD. Contrast-enhanced first-pass myocardial perfusion magnetic resonance imaging with parallel acquisition at 3.0 Tesla. *Invest Radiol*. 2007;42:352–360.
18. Treier R, Steingoetter A, Fried M, Schwizer W, Boesiger P. Optimized and combinedT1 andB1 mapping technique for fast and accurateT1 quantification in contrast-enhanced abdominal MRI. *Magn Reson Med*. 2007;57:568–576.
19. Insko EK, Bolinger L. Mapping of the radiofrequency field. *J Magn Reson, Ser A*. 1993;103:82–85.
20. Akoka S, Franconi F, Seguin F, Le Pape A. Radiofrequency map of an NMR coil by imaging. *Magn Reson Imaging*. 1993;11:437–441.
21. Yarnykh VL. Actual flip-angle imaging in the pulsed steady state: a method for rapid three-dimensional mapping of the transmitted radiofrequency field. *Magn Reson Med*. 2007;57:192–200.
22. Sacolick LI, Wiesinger F, Hancu I, Vogel MW. B1 mapping by Bloch-Siegert shift. *Magn Reson Med*. 2010;63:1315–1322.
23. Chung S, Kim D, Breton E, Axel L. Rapid B_1^+ mapping using a preconditioning RF pulse with turboFLASH readout. *Magn Reson Med*. 2010;64:439–446.
24. Nehrke K, Börnert P. DREAM-a novel approach for robust, ultrafast, multislice B1 mapping. *Magn Reson Med*. 2012;68:1517–1526.
25. Obuchowski NA, Reeves AP, Huang EP, et al. Quantitative imaging biomarkers: a review of statistical methods for computer algorithm comparisons. *Stat Methods Med Res*. 2015;24:68–106.
26. Tropp J. Image brightening in samples of high dielectric constant. *J Magn Reson*. 2004;167:12–24.
27. Jiru F, Klose U. Fast 3D radiofrequency field mapping using echo-planar imaging. *Magn Reson Med*. 2006;56:1375–1379.
28. Deoni SCL, Peters TM, Rutt BK. High-resolution T1 and T2 mapping of the brain in a clinically acceptable time with DESPOT1 and DESPOT2. *Magn Reson Med.* 2005;53:237–241.

SUPPORTING INFORMATION

Additional supporting information may be found online in the Supporting Information section at the end of the article.

Table S1: Fill solution recipes.

Table S2: Experimental verification of T_1 using DESPOT1 on a 3 T MRI (University of Southern California) and using inversion recovery on a 3 T NMR spectrometer (National Institute of Standard and Technology). Four 125 ml vials of NiCl2 solution were made to verify short and long T_1 value accuracy. For each T_1 value, we made two vials of the exact same solution. DESPOT1 method was used to measure the T_1 of the solutions at 3 T.[28] Flip angles of 2°, 3°, 5°, 7°, 10°, 12°, 15° were used for unbiased fitting of T_1 values. While DESPOT1 shows higher mean and standard deviation of T_1 values compared to NMR spectrometry, the mean of T_1 measurements are within a 9% difference margin at the relevant room temperature of 20˚C.

Table S3: Summary of spatial B_1^+ inhomogeneity in head phantoms across different scanners. While B_1^+ inhomogeneity is overall T_1 value independent, it is vendor dependent with Siemens scanners showing the smallest magnitude of deviation, followed by GE scanners, and the Philips scanner.

Table S4: Summary of B_1^+ inhomogeneity measured with DAM for the torso phantoms. Ranges of 5th percentile to 95th percentile and standard deviation (Std) of inhomogeneity are measured separately for a central and two distal slices.

Table S5: Summary of agreement of DAM with vendor specific method for head phantoms in round 1 data. Agreement is measured with Limits of Agreement (LOA) and concordance correlation coefficient (CCC). For GE, bias and reproducibility coefficient (RDC) vary strongly across scanners. Biases of the vendor method is lowest on Siemens scanners.

Table S6: Summary of agreement of DAM with vendor specific method for torso phantoms in round 1 data. As for the head phantoms, biases and RDC are strongly scanner dependent for GE systems, while they are lowest on Siemens devices.

Table S7: Summary of agreement of DAM with vendor specific method for head phantoms in round 2 data. Comparison to round 1 data in Table S7 reveals stable measurements for Philips and Siemens scanners. Results for GE scanners differ largely from round 1 measurements.

Table S8: Summary of agreement of DAM with vendor specific method for torso phantoms in round 2 data. Similar to results for the head phantom, Siemens and Philips scanners show strong consistency in repeated measurements, while agreement of DAM with vendor method varies largely on GE scanners.